Tectonophysics 714–715 (2017) 44–54

Contents lists available at ScienceDirect

Tectonophysics

journal homepage: www.elsevier.com/locate/tecto

Depth varying rupture properties during the 2015 Mw 7.8 Gorkha (Nepal) earthquake

Han Yue [a,*], Mark Simons [a], Zacharie Duputel [b], Junle Jiang [a], Eric Fielding [c], Cunren Liang [c], Susan Owen [c], Angelyn Moore [c], Bryan Riel [a], Jean Paul Ampuero [a], Sergey V. Samsonov [d]

[a] Seismological Laboratory, California Institute of Technology, Pasadena, CA, USA
[b] Institut de Physique du Globe de Strasbourg, Université de Strasbourg, EOST, CNRS, Strasbourg, France
[c] Jet Propulsion Laboratory, California Institute of Technology, Pasadena, CA, USA
[d] Canada Centre for Mapping and Earth Observation, Natural Resources Canada, Ottawa, Ontario, Canada

ARTICLE INFO

Article history:
Received 24 February 2016
Received in revised form 11 July 2016
Accepted 12 July 2016
Available online 16 July 2016

Keywords:
Gorkha earthquake
Kinematic rupture process inversion
Joint inversion
Bayesian inversion

ABSTRACT

On April 25th 2015, the Mw 7.8 Gorkha (Nepal) earthquake ruptured a portion of the Main Himalayan Thrust underlying Kathmandu and surrounding regions. We develop kinematic slip models of the Gorkha earthquake using both a regularized multi-time-window (MTW) approach and an unsmoothed Bayesian formulation, constrained by static and high rate GPS observations, synthetic aperture radar (SAR) offset images, interferometric SAR (InSAR), and teleseismic body wave records. These models indicate that Kathmandu is located near the updip limit of fault slip and approximately 20 km south of the centroid of fault slip. Fault slip propagated unilaterally along-strike in an ESE direction for approximately 140 km with a 60 km cross-strike extent. The deeper portions of the fault are characterized by a larger ratio of high frequency (0.03–0.2 Hz) to low frequency slip than the shallower portions. From both the MTW and Bayesian results, we can resolve depth variations in slip characteristics, with higher slip roughness, higher rupture velocity, longer rise time and higher complexity of subfault source time functions in the deeper extents of the rupture. The depth varying nature of rupture characteristics suggests that the up-dip portions are characterized by relatively continuous rupture, while the down-dip portions may be better characterized by a cascaded rupture. The rupture behavior and the tectonic setting indicate that the earthquake may have ruptured both fully seismically locked and a deeper transitional portions of the collision interface, analogous to what has been seen in major subduction zone earthquakes.

1. Introduction

The centroid of the April 25th 2015, the Gorkha (Nepal) earthquake (Mw 7.9, $M_0 = 8.39 \times 10^{20}$ Nm, GCMT catalog; Ekström et al., (2012)) was located within 20 km of the city of Kathmandu (Fig. 1) causing over 8000 fatalities in the city and surrounding regions (http://drrportal.gov.np/document/documentdetail/14). Ground acceleration recorded near Kathmandu had a dominant period of 4–5 s and was depleted of high frequency energy relative to that typically found for an event of this size (Galetzka et al., 2015). The recorded ground shaking of 16% g was not anticipated for an earthquake at such a small epicentral distance. Nonetheless, ground shaking in the mountainous area was sufficient to trigger a great number (>4000) of landslides (Kargel et al., 2016).

The Gorkha earthquake occurred on the Main Himalayan Thrust (MHT), which is the primary fault interface accommodating 20 ± 3 mm/yr of convergence between the Indo-Australian and Eurasian Plates (Argand, 1924; Avouac, 2003; Larson et al., 1999; Molnar, 1988). Using interseismic GPS observations (Ader et al., 2012) conclude that the MHT is locked from the surface to approximately 20 km depth. The segment of the MHT where the Gorkha earthquake occurred previously ruptured in 1833, with a rupture length of ~100 km (Bilham et al., 2001; Rana, 1935), comparable to the 2015 Gorkha earthquake. This segment is also associated with a relatively high interseismic stress loading rate (~10 kPa/yr) and active micro-seismicity (Fig. 1) (Ader et al., 2012; Pandey et al., 1995).

Studies of the kinematic rupture process of the Gorkha earthquake from back-projection of high frequency (~1 Hz) teleseismic body-wave records consistently indicate a unilateral rupture pattern (WNW-ESE) with average rupture velocity of 2.9–3.5 km/s (Avouac et al., 2015; Fan and Shearer, 2015; Wang and Mori, 2016; Zhang et al., 2016). Both static and kinematic models of the co-seismic rupture pattern constrained by a range of geodetic and teleseismic observations image an elongated unilateral rupture pattern that extends for approximately 140 km in the along-strike direction and 60 km in the cross-strike direction (Avouac et al., 2015; Galetzka et al., 2015; Lindsey et al., 2015; Wang and Fialko, 2015). Galetzka et al. (2015) also infer a

* Corresponding author.
E-mail address: hanyue@caltech.edu (H. Yue).

http://dx.doi.org/10.1016/j.tecto.2016.07.005
0040-1951/

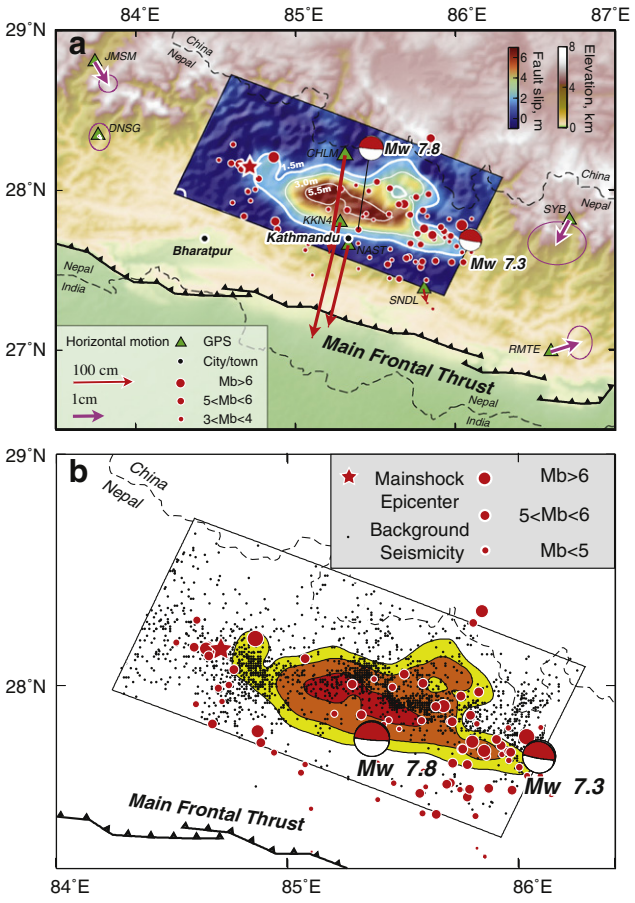

Fig. 1. (a) Map of the study area. The epicenter of the 25 April 2015 Mw 7.8 Gorkha earthquake is marked with a red-filled star. The global centroid-moment tensor solutions (GCMT) of the main shock and the Mw 7.3 aftershock are shown by red-filled focal mechanisms. The co-seismic rupture pattern from the Bayesian inversion is indicated with a blue/red color scale. Co-seismic slip counters for 1.5 m 3.0 m and 5.5 m of slip are plotted with white curves. The Main Frontal Thrust is marked with a barbed black curve. GPS stations are indicated with green-filled triangles. Co-seismic horizontal displacements for each GPS station are indicated with red and purple arrows, with ellipses indicating displacement uncertainties with 60% confidence. Two local cities are marked as black dots. Aftershock locations happened in 2 weeks after the main event are marked with red-filled circles. (b) The rupture area with co-seismic slip larger than 1.5 m, 3 m and 5.5 m are plotted as yellow, orange and red filled patches, respectively. Background seismicity (Pandey et al., 1995), located within the fault plane, is plotted in black dots.

pulse-like rupture. The existing kinematic rupture models generally show a good agreement with back-projection results in the propagation of rupture in the along strike direction (Avouac et al., 2015; Galetzka et al., 2015).

Large continental thrust earthquakes are infrequent compared with large oceanic subduction events. However, for such continental earthquakes, it is easier to obtain near field observations and thus they provide a unique opportunity to understand the source behavior of large thrust events. Here, we consider both a regularized multi-time-window (MTW) optimization approach and an unsmoothed Bayesian inversion approach to explore uncertainties in kinematic rupture parameters. We use these different approaches to resolve systematic depth-variations in slip behavior.

2. Data and methods

To investigate the kinematic rupture process during the 2015 Gorkha earthquake, we consider geodetic and seismic records at near-field and teleseismic distances.

2.1. High-rate-GPS and static-GPS data

We use the daily GPS positions to estimate the static coseismic offsets from Galetzka et al. (2015). The high-rate (hr) 5 Hz GPS time series were processed using kinematic precise point positioning with GIPSY-OASIS (Zumberge et al., 1997) and single station ambiguity resolution (Bertiger et al., 2010). Both standard and high-rate processing fixed the GPS satellite orbits and clocks to the JPL FLINN final orbit products (Desai et al., 2009). The IGS antenna phase center variations were applied to reduce errors due to antenna-specific azimuthal and elevation dependent changes in the antenna phase center (Schmid et al., 2007). Static ground displacement records of 12 static GPS stations are used in our inversion (Fig. 2). We also use 6 near field hr-GPS time series, and focus on a 3-minute window of the three-component displacement record, starting at the earthquake initiation time.

The Green's functions for hr-GPS are generated with a frequency-wavenumber integration code (Zhu and Rivera, 2002) referenced to a local 1D velocity model (Monsalve et al., 2008). Hr-GPS station NAST is located in the Kathmandu basin and thus requires a different shallow velocity structure than the other stations. To model the ground displacement at station NAST, we introduced a thin sediment layer over the average 1D velocity model. Such a low-velocity layer accounts for the amplification effect in the basin. However, we note that this modified structure cannot reproduce the basin resonance at 0.2 Hz (Ader et al., 2012; Duputel et al., 2016; Galetzka et al., 2015). To mitigate the basin effects, we apply a band-pass filter with corner frequency at 0.02 and 0.1 Hz to both the displacement record and Green's functions to reduce the impact of complex high frequency waveforms that cannot be modeled with our current Green's functions. The original hr-GPS time series is sampled at 5 sps, thus any aliasing effect to the frequency band that we are interested in is small.

2.2. Teleseismic data

The teleseismic body wave data consists of 38 *P* wave and 20 *SH* wave recordings (Fig. 2b) from stations of the Federation of Digital Seismic Networks (FDSN). We consider teleseismic data between 40° and 90° epicentral distances with high signal-to-noise ratios and good azimuthal coverage. Instrument responses are removed from the original record. We use a 2-minute-long time window starting 10 s prior to initial P or SH arrivals. Teleseismic data and Green's functions are band-pass filtered between 0.05 Hz and 0.95 Hz and down-sampled to 2 sps. We calculate teleseismic Green's functions using a reflectivity method that accounts for body wave interactions in 1-D velocity structures on both source and receiver sides (Kikuchi et al., 1993). The same local source velocity model (Monsalve et al., 2008) is used in the Green's function computation for both hr-GPS and teleseismic Green's function calculation. A typical continental model is used for the receiver side. The reference velocity model is shown in the Supplementary materials.

2.3. InSAR data

We consider 8 synthetic aperture radar (SAR) based measurements of the co-seismic displacement field produced by interferometric SAR (InSAR) and SAR pixel tracking techniques (Fig. 2d). We obtained focused radar images from the Japanese Aerospace Exploration Agency (JAXA) Advanced Land Observing Satellite 2 (ALOS2), the Copernicus Sentinel-1A satellite, and the MacDonald, Dettwiler and Associates Ltd. (MDA) RADARSAT-2 satellite. We processed the SAR data using the InSAR Scientific Computing Environment (ISCE) (Rosen et al., 2012) with prototype extensions for the special acquisition modes of the Sentinel-1 (Terrain Observation by Progressive Scans or TOPS) and ALOS-2 (ScanSAR) wide-swath images (Liang and Fielding, 2016). We consider InSAR data from two ascending ALOS-2 orbits and four descending orbits from all three satellites. The SAR pixel tracking measurements are derived from RADARSAT-2 images (see Table 1 for a complete